Monthly Notices
of the
ROYAL ASTRONOMICAL SOCIETY

MNRAS **538,** 745–754 (2025) https://doi.org/10.1093/mnras/staf333
Advance Access publication 2025 February 25

On the progenitor of the Crab Pulsar

Elvira Cruz-Cruz[1★] and C. S. Kochanek[1,2]
[1]*Department of Astronomy, The Ohio State University, 140 West 18th Avenue, Columbus, OH 43210, USA*
[2]*Center for Cosmology and Astroparticle Physics, The Ohio State University, 191 W. Woodruff Avenue, Columbus, OH 43210, USA*

Accepted 2025 February 20. Received 2025 February 19; in original form 2024 July 17

ABSTRACT

We investigate the progenitor of the Crab supernova by examining the remnant's surrounding stellar population. The Crab is interesting because of the apparently low energy and mass of the supernova remnant. We also know it was not a binary at death and that the explosion formed a neutron star. Using *Gaia* EDR3 parallaxes and photometry, we analyse stars inside a cylinder with a projected radius of 100 pc and spanning distances from $\sim$ 1600 to 2300 pc set by the 2σ uncertainties in the Crab's parallax. We also individually model the most luminous stars local to the Crab. The two most luminous stars are blue, roughly main sequence stars with masses of $\sim 11\,\mathrm{M}_{\odot}$. We estimate the stellar population's age distribution using solar metallicity `PARSEC` isochrones. The estimated age distribution of the 205 $M_{\mathrm{G}} < 0$ stars modestly favour lower mass stars, consistent with an AGB star or a lower mass binary merger as the progenitor, but statistically we cannot rule out higher masses. This may be driven by contamination due to the $\sim$ 700 pc span of the cylinder in distance.

Key words: supernovae – Hertzsprung–Russell and colour–magnitude diagrams – supernovae: general – supernovae: individual: – ISM: supernova remnants.

1 INTRODUCTION

It is important to understand the progenitors of core-collapse supernovae (ccSNe) in order to unravel the final stages of massive star evolution and its relation to supernovae and their remnants. By studying the deaths of massive stars, we can get closer to comprehending their evolution, the role of binaries, and the origins of the systems that merge and produce gravitational waves. This includes needing to distinguish the progenitors of these events, and in particular, the masses of the progenitors. Three methods have been used to constrain progenitor masses: (1) direct observations of progenitors, (2) X-ray estimates of supernovae remnant (SNR) compositions; and (3) analyses of the stellar populations local to the supernovae. The latter two methods are indirect but have the advantage that they can be used long after the explosion occurred.

The progenitors of Type II-P SNe are the best constrained thanks to direct observational detections of their progenitors in (mostly) archival *HST* data (e.g. Smartt et al. 2002a, b; Van Dyk, Li & Filippenko 2003; Maund, Smartt & Danziger 2005; Hendry et al. 2006; Li et al. 2006, 2007; Smartt et al. 2009; Maund et al. 2011; Smith et al. 2011; Van Dyk et al. 2012; Fraser et al. 2014; Maund et al. 2014). Smartt et al. (2009), using 8 mass estimates and 12 upper limits for Type II-P SN progenitors, found a minimum mass of $M < 8.5^{+1.0}_{-1.5}\mathrm{M}_{\odot}$ and a maximum mass of $M_{max} = 16.5 \pm 1.5\mathrm{M}_{\odot}$ assuming a Salpeter IMF. The progenitors to Type II-P supernovae are all red supergiants (RSG) (Smartt et al. 2009). In a later review of 18 mass estimates and 27 upper limits, Smartt (2015) found an upper mass limit for RSGs exploding as Type II SN of about $18\,\mathrm{M}_{\odot}$. Since stellar models predict that RSGs of up to $30\,\mathrm{M}_{\odot}$ undergo core-collapse and could produce Type II SN, the missing 18–30 $\mathrm{M}_{\odot}$ progenitors has been termed the red supergiant problem. Since then there has been ongoing debate about the existence of this mass range problem (e.g. Kochanek, Khan & Dai 2012; Walmswell & Eldridge 2012; Groh et al. 2013; Davies & Beasor 2018; Beasor et al. 2020; Davies & Beasor 2020; Kochanek 2020; Strotjohann, Ofek & Gal-Yam 2024). There are fewer direct detections of progenitors to Type Ibc supernovae because stripped stars tend to be optically faint and difficult to detect (e.g. Yoon et al. 2012; Eldridge et al. 2013; Folatelli et al. 2016; Johnson, Kochanek & Adams 2017; Kilpatrick et al. 2021).

A second method for understanding supernovae and their progenitors is to analyse the X-ray emission from the ejecta. Katsuda et al. (2018) made progenitor mass estimates for 33 core-collapse SNRs in our Galaxy and the Small and Large Magellanic Clouds, focusing on the Fe/Si abundance ratio. They argue that the Fe/Si ratio is the best estimate of the progenitor's CO core mass and thus the initial progenitor mass M_{ZAMS}. Katsuda et al. (2018) splits the sample into three mass bins where $M_{\mathrm{ZAMS}} < 15\,\mathrm{M}_{\odot}$, $15\,\mathrm{M}_{\odot} < M_{\mathrm{ZAMS}} < 22.5\,\mathrm{M}_{\odot}$, and $M_{\mathrm{ZAMS}} > 22.5\,\mathrm{M}_{\odot}$ to model the bin fraction with and without a mass cutoff. They argue that the observed distribution better agrees with models lacking the mass cut off implied by the red supergiant problem.

The third method is to analyse the stellar populations near both SNe and SNRs in external galaxies. The colour–magnitude diagram (CMD) of the nearby stars is modelled with isochrones to derive the local star formation history, which then provides a probability distribution for the mass of the star which exploded. For example, Jennings et al. (2014) found supernovae remnant progenitor mass distributions for M31 and M33, Auchettl et al. (2019) did so for the

---

★ E-mail: cruz-cruz.1@osu.edu

Small Magellanic Cloud, Murphy et al. (2011) did so for SN 2011dh, and Williams et al. (2014) (Díaz-Rodríguez et al. 2021) compiled progenitor mass constraints for 17 (22) historic core-collapse supernovae. Díaz-Rodríguez et al. (2021), for example, find a progenitor mass distribution with a minimum mass of $M_{\rm min} = 8.60^{+0.37}_{-0.41}\,{\rm M}_\odot$ and a slope of $\alpha = -2.61^{+1.05}_{-1.18}$.

Gaia (Gaia Collaboration 2016, 2021) makes applying the stellar population analysis method feasible in our Galaxy (Kochanek 2022). Galactic SNRs have the advantage that we frequently know the result of the explosion and the binarity of the progenitor (e.g. Ilovaisky & Lequeux 1972; Boubert et al. 2017; Kochanek 2018; Fortin et al. 2024). Accurate parallaxes allow both the selection of stars local to the SNR and the determination of their luminosities. Three dimensional dust maps (e.g. Bovy et al. 2016; Green et al. 2019) enabled by *Gaia* help to constrain the individual stellar extinctions. Kochanek (2022) and Murphy et al. (2024) successfully applied this method to the Vela pulsar. Kochanek (2022) found a progenitor mass estimate of $\leq 15\,{\rm M}_\odot$ and Murphy et al. (2024) found evidence that Vela's progenitor was the product of a binary merger. Suitable candidates for this method do require a well-constrained SNR distance, which is frequently a problem, although Kochanek, Raymond & Caldwell (2024) demonstrated a method which should provide accurate distances to any SNR with modest extinction. One good candidate is the Crab SNR where *Gaia* DR3 (Gaia Collaboration 2021) and VLBI observations of the pulsar (Lin et al. 2023) provide reasonably well-measured distances, we know that the outcome of the explosion was a neutron star (e.g. Staelin & Reifenstein 1968; Comella et al. 1969), and that the system was not a binary at death (Kochanek 2018).

The origin of the Crab SNe (i.e. ccSNe or electron capture SNe) and remnant, has long been a topic of discussion (e.g. Clark & Stephenson 1977; Davidson & Fesen 1985; Collins, Claspy & Martin 1999). The Crab nebula and pulsar are the remnants of SN 1054 (e.g. Duyvendak 1942; Mayall & Oort 1942; Staelin & Reifenstein 1968; Comella et al. 1969). The SNR appears to be low mass and have a low-kinetic energy of $\approx 10^{49}$ erg, lower than the expected kinetic energy of a core-collapse supernova $\approx 10^{51}$ erg, (e.g. MacAlpine et al. 1989; Bietenholz et al. 1991; Fesen, Shull & Hurford 1997; Smith 2003). The SN was a very luminous event with a peak absolute visual magnitude of -18 mag (e.g. Miller 1973; Trimble 1973; Chevalier 1977) that is brighter than typical Type II ccSNe (e.g. Li et al. 2011). Smith (2013) argues that the Crab was a Type IIn-P supernova caused by a sub-energetic electron-capture explosion of an 8–10 $\rm M_\odot$ super-AGB star. Electron capture SNe are generally associated with the mass range of extreme AGB stars (Miyaji et al. 1980; Nomoto et al. 1982; Nomoto 1987), although the exact mass range depends on the model (e.g. Poelarends et al. (2008) and Limongi et al. (2024) find 9.00–9.25 $\rm M_\odot$ and 8.5–9.2 $\rm M_\odot$, respectively). They are predicted to be underluminous and underenergetic (e.g. Kitaura, Janka & Hillebrandt 2006). In the Smith (2013) scenario, the high luminosity is not driven by the normal emissions of the SN, but instead by shock heating the dense circumstellar medium of the AGB star progenitor. Thus, under this hypothesis, we would expect to find a local stellar population with few or no massive stars ($\gtrsim 10\,{\rm M}_\odot$).

More recently, Omand, Sarin & Temim (2024) explored an alternate theory for the origin of SN 1054's peak luminosity. They fit a pulsar-driven supernova model to the historical observations of SN 1054's luminosity. Their model suggests an initial spin-down luminosity of the Crab pulsar of around $10^{43\text{–}45}\,{\rm erg\,s^{-1}}$ with a spin-down time-scale of 1–100 d and a low supernova explosion energy of $\sim 10^{49}$–10^{50} erg (Omand et al. 2024). This implies a high initial pulsar rotational energy of $\sim 10^{50}$ erg and an initial spin period of ~ 13 ms [other estimates of the initial spin periods are 15–20 ms (Kou & Tong 2015), and 3–5 ms (Atoyan 1999)]. They propose that the supernova underwent a 'blowout', where the pulsar wind nebula broke through the ejecta shell, leaving dense filaments behind while accelerating the outer ejecta 50–200 yr after the explosion.

Here, we apply the Kochanek (2022) approach for Vela to the Crab. In Section 2, we describe the selection of stars surrounding the Crab pulsar and the spectral energy distributions (SED) of the most luminous stars. In Section 3, we analyse the age distribution of the stars to estimate the likely mass of the Crab's progenitor. In Section 4, we discuss the results. In Section 5, we summarize our findings and potential future applications.

2 THE SURROUNDING STELLAR POPULATION

We select stars near the Crab Pulsar using *Gaia* EDR3 (Gaia Collaboration 2016, 2021) and Astroquery (Ginsburg et al. 2019). Each star is required to have a parallax and all three *Gaia* magnitudes (G, R_p and B_p). We use the position (J2000 05:34:31.947, +22:00:52.153) of the Crab pulsar from Gaia Collaboration (2021) as the centre. We use a weighted average parallax of $\varpi = 0.523 \pm 0.048$ mas ($d = 1.91^{+0.43}_{-0.30}$ kpc) for the Crab, combining the *Gaia* ($\varpi = 0.511 \pm 0.078$ mas; Gaia Collaboration 2021), and VLBI ($\varpi = 0.53 \pm 0.06$ mas; Lin et al. 2023) parallaxes. We first search for stars in a region centred on the position of the Crab with a maximum search angular size, $\theta = \sin^{-1}(R/D) = 3.58^\circ$, where D = 2 kpc and $R = 125$ pc, with parallaxes $0 < \varpi < 1$ mas. We use a magnitude limit of $G < 12$ to include stars with absolute magnitudes $M_G \leq 0$ mag and masses that are $M \gtrsim 1\,{\rm M}_\odot$.

Geometrically this search region is a truncated cone and contains 1525 stars. Next, we convert the search region from a truncated cone with a radius of $R = 125$ pc at 2 kpc into a truncated cylinder with a radius $R = 100$ pc around the Crab. From the coordinates and parallax, we form a vector ($\vec{\boldsymbol{u}}_\star$) for the position of the star. The cross product ($d_\perp = |\vec{\boldsymbol{u}}_{\rm cp} \times \vec{\boldsymbol{u}}_\star|$) with a unit vector pointing to the pulsar ($\vec{\boldsymbol{u}}_{\rm cp}$) provides the separation perpendicular to the line of sight and we keep the 225 stars with $d_\perp < R$ and parallaxes between $0.427 < \varpi < 0.619$ mas, which is the 2σ error range of the Crab's weighted average parallax. We used the 2σ range to emphasize completeness, since massive stars are rare, although the resulting length of the cylinder (~ 700 pc) is longer than desirable for minimizing contamination. We used extinction estimates for each star from the 3-dimensional (3D) `combined19` `mwdust` models (Bovy et al. 2016) which are based on Green et al. (2019) for the position of the Crab to obtain extinction corrected colours ($B_{\rm p}$–$R_{\rm p}$) and absolute magnitudes ($M_{\rm G}$). We keep the 205 stars with $-8 < M_{\rm G} < 0$, $-0.5 < B_{\rm p} - R_{\rm p} < 3.5$. In practice, there are no $M_G < -8$ mag stars in the sample. In Fig. 1, we show the CMD of these stars with the 5 most luminous stars labelled with blue stars, and PARSEC (http://stev.oapd.inaf.it/cmd) isochrones spanning $10^{7.5}$ to $10^{9.3}$ yr in steps of 0.3 dex (e.g. Bressan et al. 2012; Marigo et al. 2013, 2017; Chen et al. 2014, 2015; Tang et al. 2014; Pastorelli et al. 2019, 2020).

We first focus on these 5 most luminous stars ($M_{\rm G} < -3.5$) and fit their spectral energy distributions (SEDs) to estimate luminosities, temperatures and extinctions. We limit the SED fits to the most luminous stars because we are interested in the most massive and youngest stars local to the Crab. We use DUSTY (Elitzur & Ivezić 2001) inside a Markov Chain Monte Carlo (MCMC) driver to optimize the SED fits and their uncertainties following methods of Adams et al. (2017) and Kochanek (2022). For the coolest stars, we use MARCS (Gustafsson et al. 2008) stellar model atmospheres

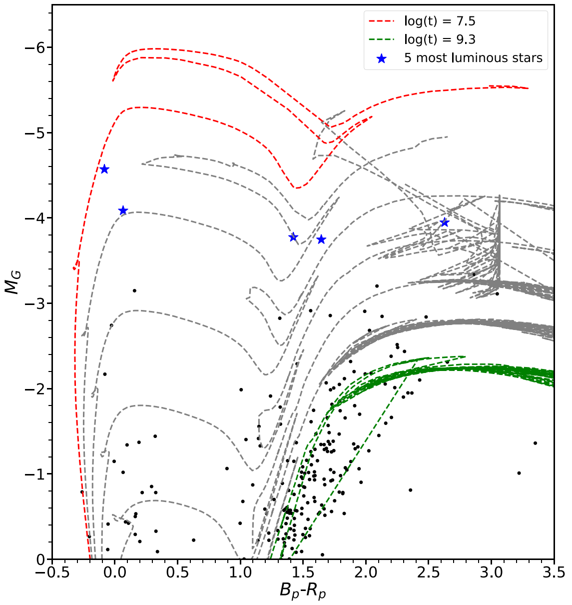

Figure 1. Extinction corrected colour–magnitude diagram of the stars local to the Crab from *Gaia* EDR3. Solar metallicity `PARSEC` isochrones are shown with dashed lines in age steps of 0.3 dex (top, red: $\log_{10}(t) = 7.5$; bottom-furthest right, green: $\log_{10}(t) = 9.3$). The blue stars are the 5 most luminous stars for which we did individual SED fits.

and Castelli & Kurucz (2003) otherwise. We use UV fluxes from Thompson et al. (1978) or Wesselius et al. (1982) if available. We use optical magnitudes from Johnson et al. (1966) and ATLAS-REFCAT (Tonry et al. 2018). The near-IR and mid-IR magnitudes were taken from 2MASS (Cutri et al. 2003) and ALLWISE (Cutri et al. 2021). We use temperature and extinction priors based on the spectral types reported in VizieR (Ochsenbein, Bauer & Marcout 2000) and the widths of the temperature and extinction prior errors were ±1000 K and ±0.1 mag.

Table 1 provides the estimated age, mass, luminosity, temperature, known or unknown spectral classification, transverse distance from the Crab pulsar and goodness of the SED fits. The age and mass constraints were obtained by finding stars on the `PARSEC` isochrones, matching the temperatures and luminosities from the SED fits to within 1σ. We then calculate the ranges, means, and dispersions reported in Table 1 from these values. We use Solar metallicity `PARSEC` isochrones with ages from $10^{6.3}$ to $10^{10.1}$ yr in steps of 0.01 dex. The SED fits yield reduced chi-squared values of $\chi^2/N_{\rm dof} \sim 2$, likely due to modest systematic errors in the models and underestimated observational errors. This has little consequence for obtaining estimates of the luminosity and temperature.

The five most luminous stars have luminosities of $10^{4.38\pm0.06}\,{\rm L}_\odot$, $10^{3.66\pm0.03}{\rm L}_\odot$, $10^{4.50\pm0.04}{\rm L}_\odot$, $10^{3.51\pm0.02}\,{\rm L}_\odot$, $10^{3.81\pm0.03}\,{\rm L}_\odot$, with masses of $11.19\,{\rm M}_\odot \pm 0.07\,{\rm M}_\odot$, $7.32\,{\rm M}_\odot \pm 0.15\,{\rm M}_\odot$, $12.33\,{\rm M}_\odot \pm 0.09\,{\rm M}_\odot$, $4.75\,{\rm M}_\odot \pm 0.06\,{\rm M}_\odot$, $4.34\,{\rm M}_\odot \pm 0.08\,{\rm M}_\odot$, respectively. The two most massive stars both lie near the main sequence and have luminous/early spectral types (O7 and B1). The other 3 stars are much less massive red giants. The spectral type reported for HD243780 (B0 E) is inconsistent with its location on the CMD and the SED model. We show the SED models in Appendix A. Fig. 2 shows the resulting SED fit temperatures and luminosities of the 5 most luminous stars on a Hertzsprung–Russell diagram.

Table 1. The luminous ($M_{\rm G} < -3.5$) stars near the Crab Pulsar.

Star	$\chi^2/N_{\rm dof}$	$\log(T_*)(K)$	$\log(L_*)({\rm L}_\odot)$	$M_*({\rm M}_\odot)$	$\overline{M_*}({\rm M}_\odot)$	$\log(t)$ (yr)	Sep (pc)	Comments
HD 36 879	1.94	4.205 ± 0.018	4.38 ± 0.06	10.74 – 11.66	11.19 ± 0.07	7.27 – 7.33	21.16	O7V C
HD 243 780	3.86	3.643 ± 0.010	3.66 ± 0.03	6.38 – 8.26	7.32 ± 0.15	7.54 – 7.81	55.84	B0 E
HD 36 547	2.18	4.283 ± 0.009	4.50 ± 0.04	11.99 – 12.54	12.33 ± 0.09	7.22 – 7.25	53.18	B1III C
IRAS 05310+2411	2.34	3.598 ± 0.007	3.51 ± 0.02	4.18 – 5.23	4.75 ± 0.06	7.97 – 8.26	70.77	No spectral type
IRAS 05361+2406	4.53	3.564 ± 0.009	3.81 ± 0.03	2.21 – 4.92	4.34 ± 0.08	8.08 – 9.05	93.38	Long period variable, no spectral type

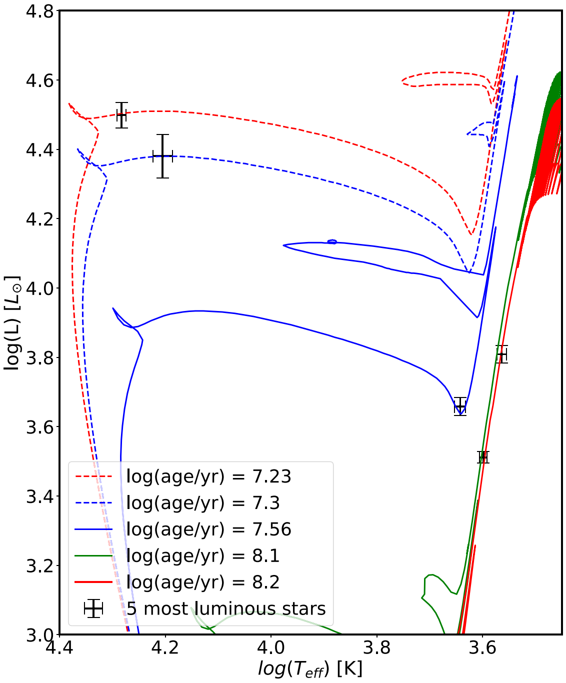

Figure 2. Estimated luminosities and temperatures of the 5 most luminous stars obtained from the SED fits as compared to PARSEC solar metallicity isochrones with ages from $10^{6.3}$ to $10^{10.1}$ yr in steps of 0.01 dex. Isochrones with the mean ages of the 5 most luminous stars are also shown.

3 PROGENITOR MASS ANALYSIS

The next step in estimating the progenitor mass of the Crab is to find the age distribution of the selected stars. We use 13 age bins ($i = 1...13$) from $10^{6.3}$ to $10^{10.1}$ yr with 0.3 dex widths (see Table 2). We assume single star evolution and solar metallicity. We randomly draw $N_{\rm trial} = 3 \times 10^8$ stars from a Salpeter IMF with a minimum mass of $M_{\rm min} = 1\,{\rm M}_\odot$ in each age bin for a total of $13 \times (3 \times 10^8)$ stars. We obtain their colour and magnitudes using the `PARSEC` isochrone models sampled with $\Delta \log t = 0.01$ dex (Bressan et al. 2012; Marigo et al. 2013; Pastorelli et al. 2020). We create stellar density maps (similar to Hess diagrams) $F_{jk}(t_i) = F^i_{jk}$, of the stars in a *Gaia* CMD where i, j, and k index the time, absolute magnitude, and colour, respectively. Each modelled star is created by uniformly selecting a time between $t_{{\rm min},i}$ and $t_{{\rm max},i}$, corresponding to a constant star formation rate for each age bin. A star is added to the density map if the chosen mass still exists on the isochrone and the star lies in the absolute magnitude range of $0.0 > M_{\rm G} > -8.0$ (index j) and the colour range $-0.5 < B_{\rm p} - R_{\rm p} < 3.5$ (index k). For each star falling within these ranges of colour and absolute magnitude, we add a 1 to the cell $[j, k]$ corresponding to their colour and magnitude. The cell sizes have widths of $\Delta(Bp - Rp) = 0.02$ and $\Delta M_{\rm G} = 0.04$ mag. We do not include either observed or model stars that are outside these colour and magnitude limits. We test the effects of this selection by creating maps that have these stars added to the edges of the stellar density bins. For example, if a star is too red it would be added to the right most edge of its density map. There are no observed stars more luminous than $M_{\rm G} = -8$ mag, but there are some stars (4) redder than $Bp - Rp > 3.5$. We found that these choices had no effect on the results (see Section 4).

We apply the `mwdust` extinction corrections to the observed stars surrounding the Crab and compare the stars to the density maps using their extinction corrected photometry (Fig. 1). We assume that these `mwdust` estimates are correct on average. We examined the effects of extinction uncertainties on the model density maps by also producing density maps with random Gaussian extinctions of $\sigma_{E(B-V)} = 0.01$, 0.03 and 0.1 mag added to each trial star.

For a constant star formation rate (SFR), the formation rate by mass for $M > M_{\rm min}$ is

$$\frac{dN}{dMdt} = \frac{(x-2)SFR}{M_{\rm min}^2}\left(\frac{M}{M_{\rm min}}\right)^{-x} \qquad (1)$$

with $x = 2.35$ and a mean mass of $\langle M\rangle = (x-1)M_{min}/(x-2) = 3.86\,{\rm M}_\odot$ for $M_{\rm min} = 1\,{\rm M}_\odot$. The age bins are in logarithmic time intervals, $t_{{\rm min},i} < t < t_{{\rm max},i}$, where $\Delta t = t_{{\rm max},i} - t_{{\rm min},i}$. Since the SFR_i is constant, the number of $M > M_{\rm min}$ stars formed in each interval is $N_{\rm i} = SFR_i \Delta t_i/\langle M\rangle$. The number of stars that die in a short time interval δt today is

$$N_i\frac{\delta t}{\Delta t_i}\left[\left(\frac{M(t_{{\rm min},i})}{M_{\rm min}}\right)^{(1-x)} - \left(\frac{M(t_{{\rm max},i})}{M_{\rm min}}\right)^{(1-x)}\right] = N_i S_i \delta t \qquad (2)$$

where M(t) is the most massive surviving star on the isochrone, and $S_i\delta t$ is the fraction of $M > M_{\rm min}$ stars that died in the last δt years. A full derivation of equation (2) is in Appendix B.

The observed stars can be placed on the absolute magnitude and colour grid in the same manner, with $N^\star_{jk}$ stars in a pixel and $\sum_{jk} N^\star_{jk} = N^\star = 205$. The number of model stars in a given magnitude and colour bin is $N_{jk} = \sum_i \alpha_i F^i_{jk}$, where α_i is proportional to the star formation rate of age bin i, and the model has a total of $N = \sum_{jk} N_{jk}$ stars. The Poisson probability of finding the observed number of stars in a bin of colour and magnitude is

$$\frac{N_{jk}^{N^\star_{jk}} e^{-N_{jk}}}{N^\star_{jk}!}, \qquad (3)$$

so the logarithm of the likelihood for all $N^\star$ stars is

$$\ln L = \sum_{jk} \ln\left(rN_{jk}^{N^\star_{jk}}\right) - \sum_{jk} rN_{jk}, \qquad (4)$$

where the first term is the sum over bins containing stars and the second is the sum over all bins. We discard the factorial $N^\star_{jk}!$ because the calculation depends only on likelihood differences and not the absolute likelihood. Empty cells of N_{jk} are filled with a small number (1×10^{-32}) to avoid numerical problems.

We introduced a ‘re-normalization’ factor r in equation (4). Equation (4) with $r \equiv 1$ will include Poisson fluctuations in N relative to $N^\star$. However, we really want the probability for how the $N^\star$ stars are divided over the 13 age bins. If we choose

$$r = N^\star\left[\sum_{jk}\sum_{i} \alpha_i F^i_{jk}\right]^{-1}, \qquad (5)$$

and then re-normalize $\alpha_i \rightarrow r\alpha_i = \rho_i$ so that $\sum_{jk}\sum_i \rho_i F^i_{jk} \equiv N \equiv N^\star$, the likelihood becomes the multinomial likelihood for how to divide the $N^\star$ stars over the age bins. Some age bins are susceptible to $\log(N_i) \rightarrow -\infty$. To prevent such numerical divergences, we add a weak prior of

$$-\lambda^{-2}\sum_i\left[\ln\left(\frac{\alpha_i\Delta t_{i+1}}{\alpha_{i+1}\Delta t_i}\right)\right]^2 - \lambda^{-1}\sum_i\left[\ln\left(\frac{\alpha_i}{\alpha_0}\right)\right]^2, \qquad (6)$$

where both terms of the equation have $\lambda = \ln 10^3 = 6.91$. The first term adds a penalty of unity to the likelihood if adjacent bins have star formation rates that differ by a factor of 1000. The second term penalizes not distributing the observed stars uniformly over the age bins.

Table 2. The distribution of the observed stars (column: $N^\star$, Fig. 4) across the age bins (column: $t_{\rm min} - t_{\rm max}$), the implied star formation rate (column: $N^\star/\Delta t_i$, Fig. 5), and the probability of stars dying in the last 10^5 yr (column: $N_i S_i \delta t$, Fig. 8).

$t_{\rm min} - t_{\rm max}$ (yr)	$N^\star$	$N^\star/\Delta t_i$ ($M > 1{\rm M}_\odot$/1 Gyr)	$N_i S_i \delta t[\delta t = 10^5$ yr]
$10^{6.3} - 10^{6.6}$	0.85 ± 0.81	2788 ± 2647	0.0013 ± 0.0012
$10^{6.6} - 10^{6.9}$	0.89 ± 0.82	1547 ± 1439	0.0014 ± 0.0013
$10^{6.9} - 10^{7.2}$	1.15 ± 1.04	1080 ± 976	0.0016 ± 0.0014
$10^{7.2} - 10^{7.5}$	1.35 ± 1.14	707 ± 597	0.0014 ± 0.0011
$10^{7.5} - 10^{7.8}$	3.73 ± 1.94	1135 ± 592	0.0033 ± 0.0017
$10^{7.8} - 10^{8.1}$	4.56 ± 2.19	861 ± 414	0.0034 ± 0.0016
$10^{8.1} - 10^{8.4}$	7.38 ± 2.83	906 ± 348	0.0046 ± 0.0017
$10^{8.4} - 10^{8.7}$	26.70 ± 5.08	2205 ± 419	0.0146 ± 0.0027
$10^{8.7} - 10^{9.0}$	19.01 ± 4.61	2307 ± 559	0.0203 ± 0.0049
$10^{9.0} - 10^{9.3}$	37.50 ± 6.51	6188 ± 1075	0.0958 ± 0.0166
$10^{9.3} - 10^{9.6}$	61.38 ± 7.81	7572 ± 964	0.1488 ± 0.0189
$10^{9.6} - 10^{9.9}$	18.06 ± 5.06	1981 ± 555	0.0413 ± 0.0115
$10^{9.9} - 10^{10.1}$	18.48 ± 4.46	3642 ± 880	0.0572 ± 0.0138

We calculate the number of deaths in a time range δt with $N_i S_i \delta t$, where S_i is independent of δt. We want to find the probability that the progenitor was born from age bin i versus j, and therefore use the normalized probability for each age bin of

$$\frac{P_i}{P_{\rm tot}} = \frac{N_i S_i}{\sum_{\rm all} N_i S_i}, \tag{7}$$

which is independent of δt and has a total probability of unity.

We optimize the likelihood (equation 4) and estimate the uncertainties using the Monte Carlo Markov Chain (MCMC) driver in the EMCEEPYTHON package (Foreman-Mackey et al. 2013), with $\log \alpha_i$ as the fit parameters. We use 300 walkers each with a chain length 10 000. We discard the first 1000 entries of each walker chain for determining uncertainties. Within the MCMC driver, these $\log \alpha_i$ are re-normalized (equation 5) before calculating the likelihood. We then use the MCMC chain results to derive the probability distributions shown in Figs 4–9.

4 RESULTS

Fig. 3 shows the resulting density contours for the distribution of the model stars in the CMD for the maximum likelihood model. The purple (magenta) contour lines show the low (high) stellar densities. The maximum densities lie along the main sequence and the red giant branch as expected and largely encompasses the observed stars.

Figs 4 and 5 show two different ways to view the distribution of stars in age. Fig. 4 shows the distribution of the $N^\star = 205$ modeled stars over the age bins. The total number of stars is exactly equal to 205 because of the renormalization in equation (5). The fourth youngest age bin is $10^{7.2}$–$10^{7.5}$ yr, which corresponds to the mass ranges of 9.1 M$_\odot$–13.1 M$_\odot$, contains 1 star, and the next age bin $10^{7.5}$–$10^{7.8}$ yr (6.5–9.1M$_\odot$) contains about 4 stars. Consistent with Fig. 3, there are very few high-mass stars in the region local to the Crab. The next two age bins corresponding to ages $10^{7.8} - 10^{8.4}$ yr (3.7–6.5 M$_\odot$) contain about 12 stars. The eighth oldest age bin ($10^{8.4} - 10^{8.7}$ yr: 2.9–3.7 M$_\odot$) has about 27 stars. Fig. 4 also shows the estimated ages of the 5 most luminous stars from the SED fits as red arrows. The two youngest stars fall on the edge of the third youngest age bin ($10^{6.9}$–$10^{7.2}$ yr) and the fourth youngest age bin ($10^{7.2}$–$10^{7.5}$ yr or 9.1–13.1 M$_\odot$), which is also consistent with the number of stars found by our Monte Carlo model (see Table 2). Fig. 5 shows the number N_i of $M > 1{\rm M}_\odot$ stars formed per 10^9 years as a function of age. This is simply the observed number of stars (Fig. 4) divided by the fraction of the Monte Carlo trials leading to a star on the density grid and the temporal width of the bin. Fig. 5 corresponds to the star formation history of the stars surrounding the Crab. The normalization to the number of $M > 1{\rm M}_\odot$ stars formed per billion years is arbitrary.

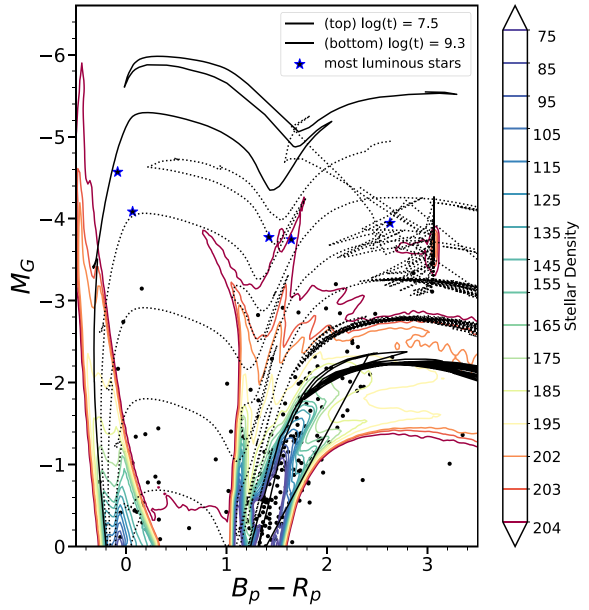

Figure 3. The black dots are the extinction corrected *Gaia* CMD of the stars near the Crab, and the curves are the solar metallicity PARSEC isochrones with ages from $10^{7.5}$ (top black) to $10^{9.3}$ yr (bottom black) in steps of 0.3 dex. The model density contours are drawn at the level which encompasses the number of stars shown on the scale bar. The blue (larger) stars are the 5 most luminous stars near the Crab.

Fig. 6 compares the result in Fig. 4 to the result when we include a scatter in the extinction corrections of $\sigma_{\rm ext} = 0.1, 0.03$, or 0.01 mag, and Fig. 7 does the same but also includes stars which are too red or too blue on the grid edges. The qualitative structure of Fig. 4 is little changed by these variations.

Figs 8 and 9 show the differential and integral distributions in age of the number of stars expected to have died in the last $\delta t = 10^5$ yr. The probabilities are low because if we took a random volume with this stellar age distribution, the probability of finding an SNR would

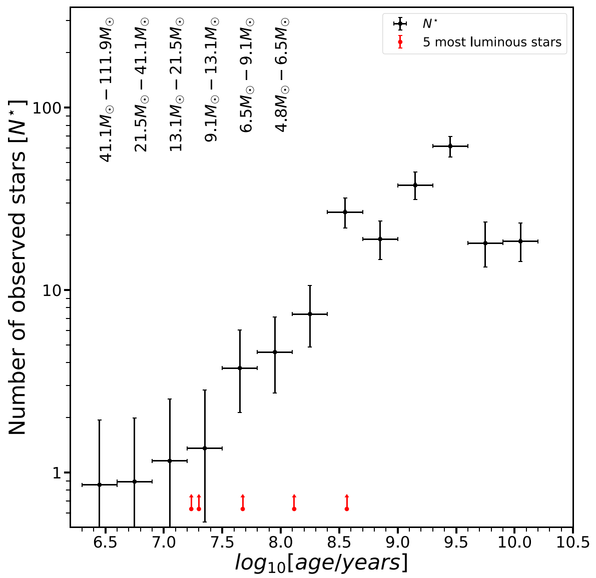

Figure 4. The number of observed stars assigned to each age bin (black points), where the horizontal bar shows the width of the bin in age. The mass range for each age bin is listed at the top left of the plot. The points and vertical error bars are the median and 16 and 84 percentile ranges of the number of stars associates with each age bin. The red arrows show the estimated ages of the 5 individually modelled stars.

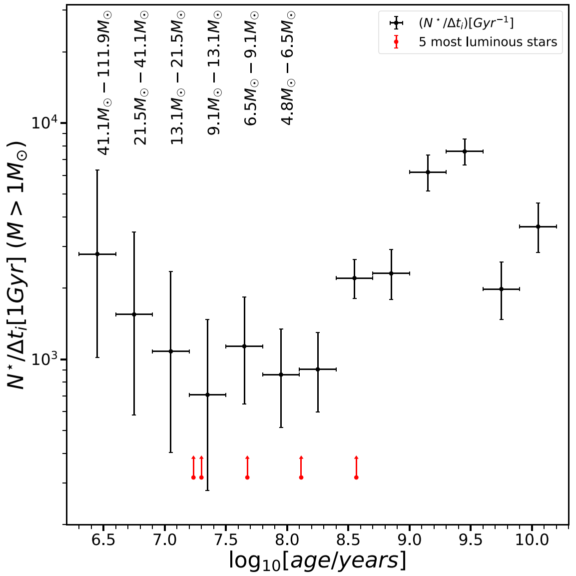

Figure 5. The number $N_i^\star$ of $M > 1\,\mathrm{M}_\odot$ stars formed in each age bin per 10^9 yr. This corresponds to the number of observed stars shown in Fig. 4 divided by the fraction of the Monte Carlo trials leading to a star on the density grid and the temporal age bin width, Δt_i (in units of $1\,\mathrm{Gyr} = 10^9$ yr). The horizontal errors are the 0.3 dex widths of the age bins. The red arrows (bottom) are the estimated ages of the 5 most luminous stars.

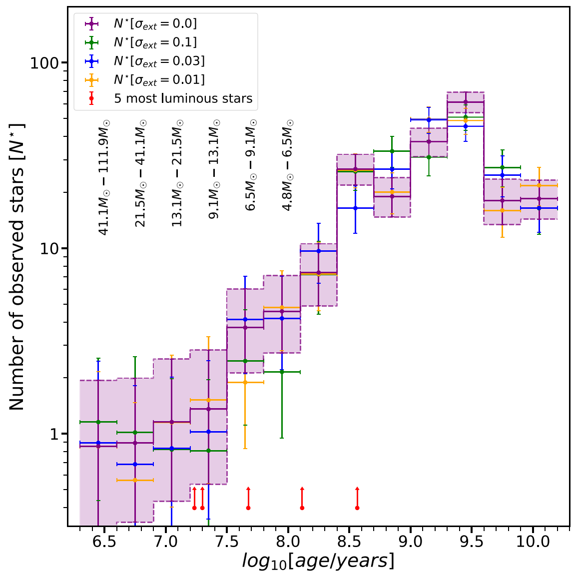

Figure 6. The model distributions of the observed stars in the age bins using stellar density grids with an extinction scatter of $\sigma_{ext} = 0.1, 0.03, 0.01$ (orange, green, and blue, respectively). The number of observed stars in Fig. 4 are plotted in purple (shaded region), $\sigma_{\rm ext} = 0.0$. The red arrows show the estimated ages of the 5 most luminous stars.

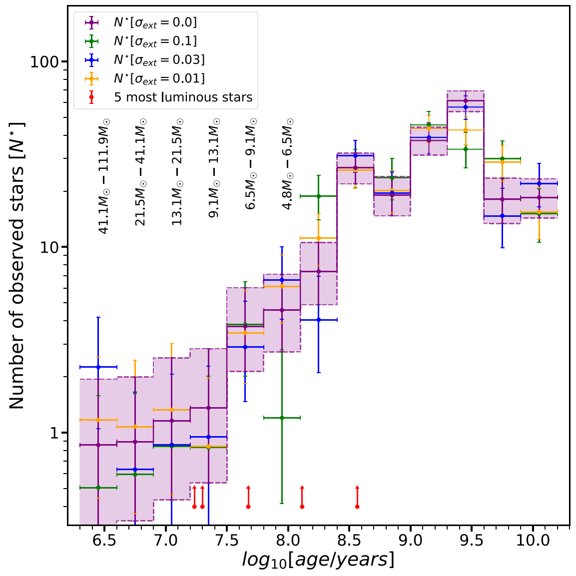

Figure 7. The model distribution of the observed stars across the age bins using stellar density maps with the alternate treatment of colour edge effects and $\sigma_{ext} = 0.1, 0.03, 0.01$, shown in orange, green, and blue, respectively. The vertical error bars span the 16th and 84th percentiles. The number of observed stars with the standard treatment of edge effects and no extinction scatter ($\sigma_{\rm ext} = 0.0$) are plotted in purple (shaded region). The red arrows are the estimated ages of the 5 most luminous stars.

be very low. By selecting the volume to contain an SNR, it is no longer random. This selection effect only affects the absolute probabilities and not the relative probabilities. Formally, we find that lower mass progenitors are favoured, but the probability contrast between the lower and higher masses does not allow a very strong limit. If we focus on the differential probability, the age bins corresponding to stars which might be electron capture supernovae either directly or as a binary merger product (the $10^{7.2}$–$10^{7.8}$yr age bins with a mass range of 6.5–13.1 $\mathrm{M}_\odot$), they have median likelihoods roughly 5 times those of the higher mass ($\geq 13.1\mathrm{M}_\odot$) bins (see Table 2). However, if we consider the integral probability distribution over this same age range, these two bins encompass only 64 per cent of the probability. If we include the next lower age bin ($10^{7.8}$–$10^{8.1}$ yr with masses 4.8–6.5 $\mathrm{M}_\odot$), this increases to 76 per cent of

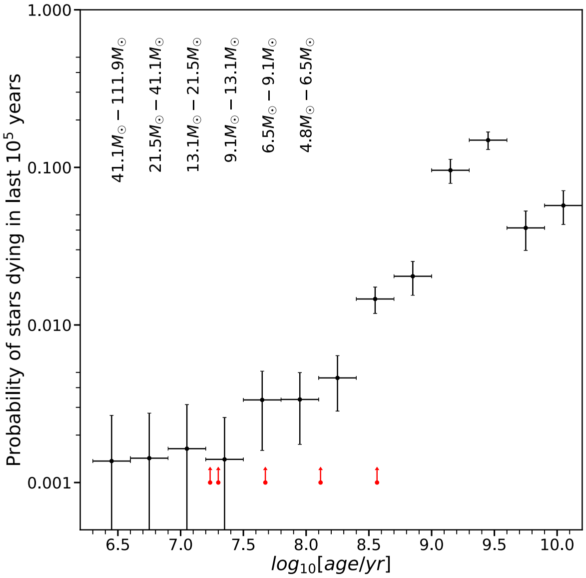

Figure 8. The probability of the number of stellar deaths over the last 10^5 yr for each age bin are shown with points with their 1σ confidence range (vertical error bars). The horizontal error bars span the 0.3 dex age bin widths. The red arrows show the ages of the 5 most luminous stars.

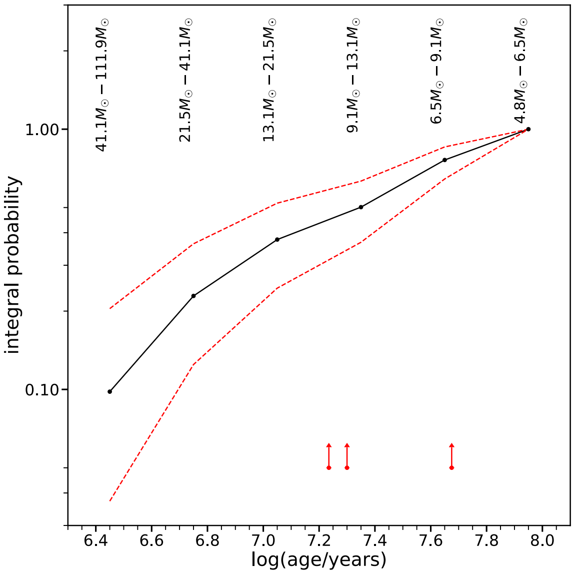

Figure 9. Integral probability distribution of the number of stellar deaths as a function of age. The red dashed lines are the 1σ confidence range for the median number of stellar deaths within each age bin. The arrows are the age estimates of the 3 most luminous stars. The distribution is truncated on the oldest age bin that can produce a ccSN, albeit through the explosion of a merger remnant.

the probability. Essentially, the dynamic range of the differential probability distribution is simply not large enough to strongly rule out higher-mass progenitors (e.g. there is a ~ 20 per cent chance of being from the two youngest bins, corresponding to masses $M \geq 21.5$). However, the absence of any luminous stars for age bins younger than $10^{7.2}$ yr suggests that these younger ages should be disfavored.

5 DISCUSSION

We examine the properties of the 205 stars with $-8 < M_{\rm G} < 0$ mag and $-0.5 < Bp - Rp < 3.5$ in a volume surrounding the Crab SNR. If we examine the five most luminous stars, we find that the two most luminous, HD 36 879 and HD 36547, have luminosities, masses and ages of roughly $10^{4.38\pm0.06}\,{\rm L}_\odot(10^{4.50\pm0.04}\,{\rm L}_\odot)$, $11.19\,{\rm M}_\odot \pm 0.07\,{\rm M}_\odot(12.33\,{\rm M}_\odot \pm 0.09\,{\rm M}_\odot)$, and $10^{7.30}$ yr ($10^{7.23}$ yr). Both are main sequence or perhaps slightly evolved blue stars. If we analyse the overall age distribution of all these stars and estimate the likely age distribution of stars which will have recently died, we find modest evidence in favour of lower mass stars, consistent with the proposal that the progenitor was an extreme AGB star leading to an electron capture supernova. The age bin where the progenitor could be the explosion of a binary merger (Zapartas et al. 2017) is roughly likely as the age bin corresponding to a directly formed AGB star. This is interesting since the Crab was not a binary at death (Kochanek 2018), but almost all massive stars start in binary or high order systems (e.g. Sana et al. 2012; Moe & Di Stefano 2013). Unfortunately, the probability distribution does not drop sufficiently rapidly towards younger, higher mass progenitors to make a strong statistical case for this scenario. These results are stable with respect to the treatment of edge effects and allowing for noise in the stellar extinction estimates. One problem is that the parallax of the Crab is still relatively uncertain. We used a distance range of roughly ~ 700 pc (2σ on the parallax) to have a complete sample of stars. Using a 1σ parallax range (~ 350 pc) leads to a sample of ~ 100 stars. This choice would have less contamination, but would be very incomplete. Kochanek (2022) explores these issues for the stellar populations around Vela.

The main problem for wide spread use of this approach for Galactic SNRs is that the distances to the SNRs are generally even more uncertain than that of the Crab. Kochanek et al. (2024) demonstrate a new method for estimating distances using multiobject high-resolution spectrographs, like Hectochelle (Szentgyorgyi et al. 2011) on the MMT, to search for the appearance of high velocity absorption features in stars behind the SNR that can provide distances to the typical SNR where there is no parallax for a remnant. Even in cases like the Crab with a parallax measurement, this approach may still do better than a direct parallax because it can average over the parallaxes of multiple stars rather than a single object. Well-constrained distances to SNRs would allow the analysis of their surrounding stellar populations to estimate many more progenitor masses. Some SNRs of particular interest are the ones which are presently interacting binaries (SS 433, HESS J0632+057, 1FGL J1018.6−5856; Blundell & Bowler 2004; Hinton et al. 2009; Corbet et al. 2011; Fermi LAT Collaboration 2012, respectively) and the one relatively clear case of a binary unbound in the supernova (S147, Dinçel et al. 2015; Kochanek 2021). In addition to being interesting as a study of progenitors known to be in binaries, the parallax of the companion star solves the distance uncertainty problem.

ACKNOWLEDGEMENTS

Elvira Cruz-Cruz is supported by NASA FINESST Fellowship 80NSSC23K1444. Christopher S. Kochanek is supported by NSF grants AST-2307385 and AST-2407206. This research has made use of the VizieR catalogue access tool, CDS, Strasbourg, France (Ochsenbein 1996). This work has made use of data from the European Space Agency (ESA) mission *Gaia* (https://www.cosmos.esa.int/gaia), processed by the *Gaia* Data Processing and Analysis Consortium (DPAC, https://www.cosmos.esa.int/web/gaia/dpac/consortium). Funding for the DPAC has been provided by national institutions, in particular the institutions participating in the *Gaia* Multilateral Agreement.

In loving memory of my *Abuelita Eulalia Ledezma-Valdez*, the only progenitor I had the privilege of knowing. Like a distant star whose light still reaches us, her wisdom and love continue to illuminate my path.

DATA AVAILABILITY STATEMENT

All *Gaia* (Gaia Collaboration 2016, 2021) data used in this analysis are publicly available through the *Gaia* Archive at the European Space Agency (ESA) website (https://gea.esac.esa.int/archive/), with the primary data set being *Gaia* EDR3. The `PARSEC` isochrones are publicly available at http://stev.oapd.inaf.it/cmd.

REFERENCES

Adams S. M., Kochanek C. S., Gerke J. R., Stanek K. Z., Dai X., 2017, MNRAS, 468, 4968

Atoyan A. M., 1999, A&A, 346, L49

Auchettl K., Lopez L. A., Badenes C., Ramirez-Ruiz E., Beacom J. F., Holland-Ashford T., 2019, ApJ, 871, 64

Beasor E. R., Davies B., Smith N., van Loon J. T., Gehrz R. D., Figer D. F., 2020, MNRAS, 492, 5994

Bietenholz M. F., Kronberg P. P., Hogg D. E., Wilson A. S., 1991, ApJ, 373, L59

Blundell K. M., Bowler M. G., 2004, ApJ, 616, L159

Boubert D., Fraser M., Evans N. W., Green D. A., Izzard R. G., 2017, A&A, 606, A14

Bovy J., Rix H.-W., Green G. M., Schlafly E. F., Finkbeiner D. P., 2016, ApJ, 818, 130

Bressan A., Marigo P., Girardi L., Salasnich B., Dal Cero C., Rubele S., Nanni A., 2012, MNRAS, 427, 127

Castelli F., Kurucz R. L., 2003, in Piskunov N., Weiss W. W., Gray D. F., eds, Vol. 210, Modelling of Stellar Atmospheres. p. A20, preprint (arXiv:astro-ph/0405087)

Chen Y., Girardi L., Bressan A., Marigo P., Barbieri M., Kong X., 2014, MNRAS, 444, 2525

Chen Y., Bressan A., Girardi L., Marigo P., Kong X., Lanza A., 2015, MNRAS, 452, 1068

Chevalier R. A., 1977, in Schramm D. N., ed., Astrophysics and Space Science Library Vol. 66, Supernovae. p. 53

Clark D. H., Stephenson F. R., 1977, The historical supernovae

Collins George W. I., Claspy W. P., Martin J. C., 1999, PASP, 111, 871

Comella J. M., Craft H. D., Lovelace R. V. E., Sutton J. M., 1969, Nature, 221, 453

Corbet R. H. D. et al., 2011, Astron. Telegram, 3221, 1

Cutri R. M. et al., 2003, 2MASS All Sky Catalog of point sources.

Cutri R. M. et al.VizieR Online Data Catalog: AllWISE Data Release (Cutri+ 2013), Provided by the SAO/NASA Astrophysics Data System 2021

Davidson K., Fesen R. A., 1985, ARA&A, 23, 119

Davies B., Beasor E. R., 2018, MNRAS, 474, 2116

Davies B., Beasor E. R., 2020, MNRAS, 496, L142

Díaz-Rodríguez M., Murphy J. W., Williams B. F., Dalcanton J. J., Dolphin A. E., 2021, MNRAS, 506, 781

Dinçel B., Neuhäuser R., Yerli S. K., Ankay A., Tetzlaff N., Torres G., Mugrauer M., 2015, MNRAS, 448, 3196

Duyvendak J. J. L., 1942, PASP, 54, 91

Eldridge J. J., Fraser M., Smartt S. J., Maund J. R., Crockett R. M., 2013, MNRAS, 436, 774

Elitzur M., Ivezić Ž., 2001, MNRAS, 327, 403

Fermi LAT Collaboration, 2012, Science, 335, 189

Fesen R. A., Shull J. M., Hurford A. P., 1997, AJ, 113, 354

Folatelli G. et al., 2016, ApJ, 825, L22

Foreman-Mackey D., Hogg D. W., Lang D., Goodman J., 2013, PASP, 125, 306

Fortin F., Kalsi A., García F., Simaz-Bunzel A., Chaty S., 2024, A&A, 684, A124

Fraser M. et al., 2014, MNRAS, 439, L56

Gaia Collaboration, 2016, A&A, 595, A1

Gaia Collaboration, 2021, A&A, 649, A1

Ginsburg A. et al., 2019, AJ, 157, 98

Green G. M., Schlafly E., Zucker C., Speagle J. S., Finkbeiner D., 2019, ApJ, 887, 93

Groh J. H., Meynet G., Georgy C., Ekström S., 2013, A&A, 558, A131

Gustafsson B., Edvardsson B., Eriksson K., Jørgensen U. G., Nordlund Å., Plez B., 2008, A&A, 486, 951

Hendry M. A. et al., 2006, MNRAS, 369, 1303

Hinton J. A. et al., 2009, ApJ, 690, L101

Ilovaisky S. A., Lequeux J., 1972, A&A, 18, 169

Jennings Z. G., Williams B. F., Murphy J. W., Dalcanton J. J., Gilbert K. M., Dolphin A. E., Weisz D. R., Fouesneau M., 2014, ApJ, 795, 170

Johnson H. L., Mitchell R. I., Iriarte B., Wisniewski W. Z., 1966, Commun. Lunar Planet. Lab., 4, 99

Johnson S. A., Kochanek C. S., Adams S. M., 2017, MNRAS, 472, 3115

Katsuda S., Takiwaki T., Tominaga N., Moriya T. J., Nakamura K., 2018, ApJ, 863, 127

Kilpatrick C. D. et al., 2021, MNRAS, 504, 2073

Kitaura F. S., Janka H. T., Hillebrandt W., 2006, A&A, 450, 345

Kochanek C. S., 2018, MNRAS, 473, 1633

Kochanek C. S., 2020, MNRAS, 493, 4945

Kochanek C. S., 2021, MNRAS, 507, 5832

Kochanek C. S., 2022, MNRAS, 511, 3428

Kochanek C. S., Khan R., Dai X., 2012, ApJ, 759, 20

Kochanek C. S., Raymond J. C., Caldwell N., 2024, ApJ, 968, 9

Kou F. F., Tong H., 2015, MNRAS, 450, 1990

Li W., Van Dyk S. D., Filippenko A. V., Cuillandre J.-C., Jha S., Bloom J. S., Riess A. G., Livio M., 2006, ApJ, 641, 1060

Li W., Wang X., Van Dyk S. D., Cuillandre J.-C., Foley R. J., Filippenko A. V., 2007, ApJ, 661, 1013

Li W. et al., 2011, MNRAS, 412, 1441

Limongi M., Roberti L., Chieffi A., Nomoto K., 2024, ApJS, 270, 29

Lin R., van Kerkwijk M. H., Kirsten F., Pen U.-L., Deller A. T., 2023, ApJ, 952, 161

MacAlpine G. M., McGaugh S. S., Mazzarella J. M., Uomoto A., 1989, ApJ, 342, 364

Marigo P., Bressan A., Nanni A., Girardi L., Pumo M. L., 2013, MNRAS, 434, 488

Marigo P. et al., 2017, ApJ, 835, 77

Maund J. R., Smartt S. J., Danziger I. J., 2005, MNRAS, 364, L33

Maund J. R. et al., 2011, ApJ, 739, L37

Maund J. R., Mattila S., Ramirez-Ruiz E., Eldridge J. J., 2014, MNRAS, 438, 1577

Mayall N. U., Oort J. H., 1942, PASP, 54, 95

Miller J. S., 1973, ApJ, 180, L83

Miyaji S., Nomoto K., Yokoi K., Sugimoto D., 1980, PASJ, 32, 303

Moe M., Di Stefano R., 2013, ApJ, 778, 95

Murphy J. W., Jennings Z. G., Williams B., Dalcanton J. J., Dolphin A. E., 2011, ApJ, 742, L4

Murphy J. W., Barrientos A. F., Andrae R., Guzman J., Williams B. F., Dalcanton J. J., Koplitz B., 2024, preprint (arXiv:2406.04075)

Nomoto K., 1987, ApJ, 322, 206

Nomoto K., Sparks W. M., Fesen R. A., Gull T. R., Miyaji S., Sugimoto D., 1982, Nature, 299, 803

Ochsenbein F., 1996, The VizieR database of astronomical catalogues, https://vizier.cds.unistra.fr

Ochsenbein F., Bauer P., Marcout J., 2000, A&AS, 143, 23

Omand C. M. B., Sarin N., Temim T., 2024, MNRAS, 536, 408

Pastorelli G. et al., 2019, MNRAS, 485, 5666

Pastorelli G. et al., 2020, MNRAS, 498, 3283

Poelarends A. J. T., Herwig F., Langer N., Heger A., 2008, ApJ, 675, 614

Sana H. et al., 2012, Science, 337, 444

Smartt S. J., 2015, PASA, 32, e016
Smartt S. J., Gilmore G. F., Tout C. A., Hodgkin S. T., 2002a, ApJ, 565, 1089
Smartt S. J., Vreeswijk P. M., Ramirez-Ruiz E., Gilmore G. F., Meikle W. P. S., Ferguson A. M. N., Knapen J. H., 2002b, ApJ, 572, L147
Smartt S. J., Eldridge J. J., Crockett R. M., Maund J. R., 2009, MNRAS, 395, 1409
Smith N., 2003, MNRAS, 346, 885
Smith N., 2013, MNRAS, 434, 102
Smith N. et al., 2011, ApJ, 732, 63
Staelin D. H., Reifenstein Edward C. I., 1968, Science, 162, 1481
Strotjohann N. L., Ofek E. O., Gal-Yam A., 2024, ApJ, 964, L27
Szentgyorgyi A. et al., 2011, PASP, 123, 1188
Tang J., Bressan A., Rosenfield P., Slemer A., Marigo P., Girardi L., Bianchi L., 2014, MNRAS, 445, 4287
Thompson G. I., Nandy K., Jamar C., Monfils A., Houziaux L., Carnochan D. J., Wilson R., 1978, Catalogue of stellar ultraviolet fluxes: a compilation of absolute stellar fluxes measured by the Sky Survey Telescope (S2/68) aboard the ESRO satellite TD-1 /
Tonry J. L. et al., 2018, ApJ, 867, 105
Trimble V., 1973, PASP, 85, 579
Van Dyk S. D., Li W., Filippenko A. V., 2003, PASP, 115, 1289
Van Dyk S. D. et al., 2012, ApJ, 756, 131
Walmswell J. J., Eldridge J. J., 2012, MNRAS, 419, 2054
Wesselius P. R., van Duinen R. J., de Jonge A. R. W., Aalders J. W. G., Luinge W., Wildeman K. J., 1982, A&AS, 49, 427
Williams B. F., Peterson S., Murphy J., Gilbert K., Dalcanton J. J., Dolphin A. E., Jennings Z. G., 2014, ApJ, 791, 105
Yoon S. C., Gräfener G., Vink J. S., Kozyreva A., Izzard R. G., 2012, A&A, 544, L11
Zapartas E. et al., 2017, A&A, 601, A29

APPENDIX A: SED FIT RESULTS

Figs A1 through A5 show the SED models for each of the 5 most luminous stars found near the Crab.

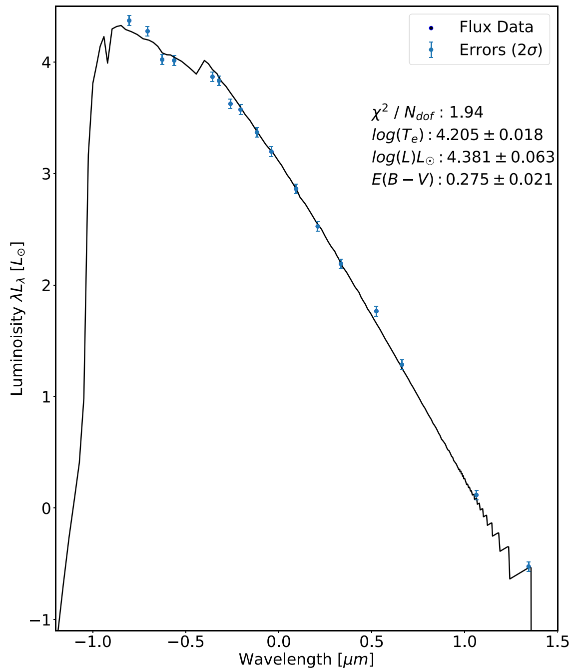

Figure A1. The SED of the O7V(n)(f)z C star HD 36879.

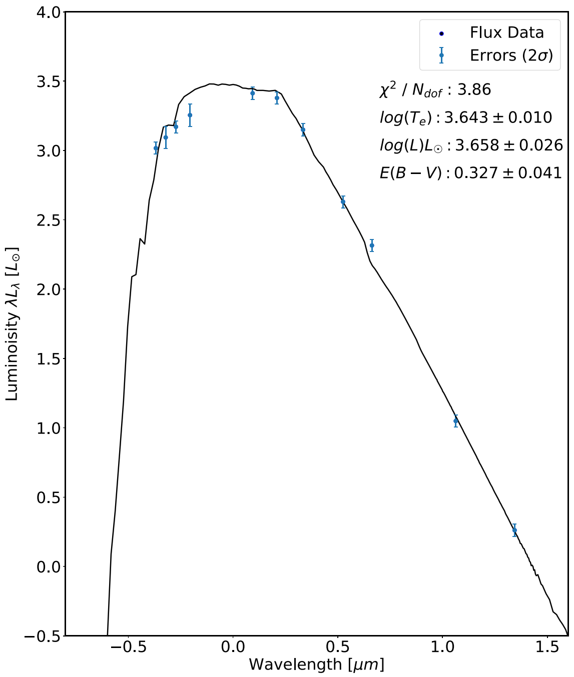

Figure A2. The SED of the B0 E Star HD 243780.

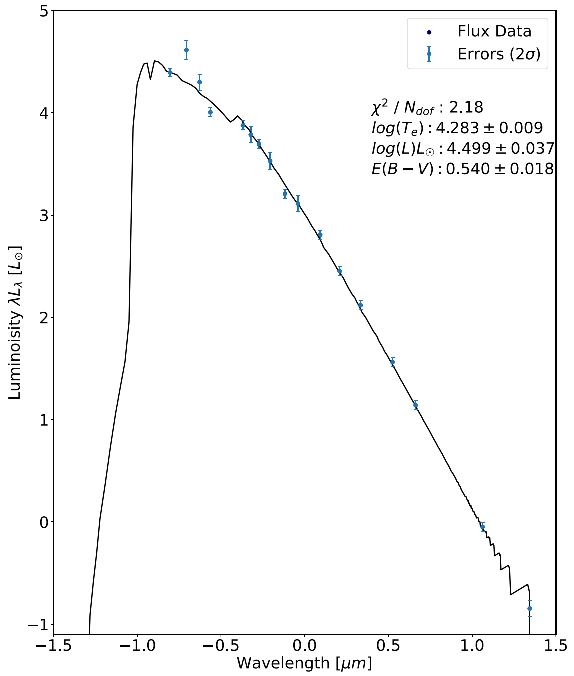

Figure A3. The SED of the B1III C star HD 36547.

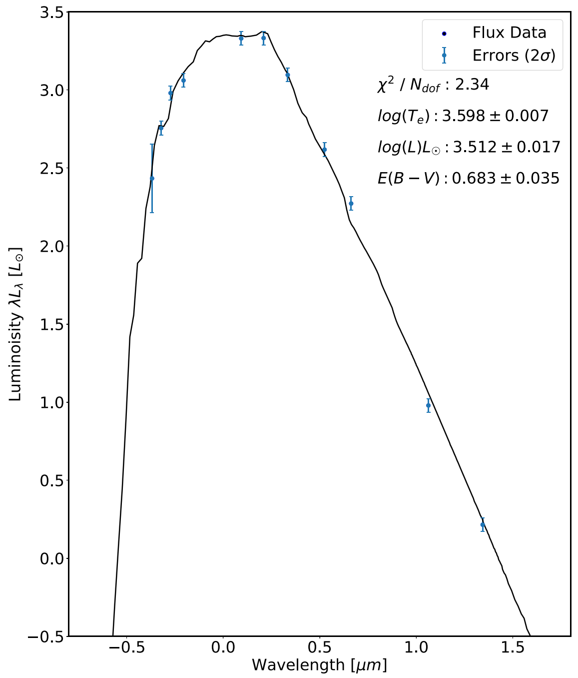

Figure A4. The SED of IRAS 5310 + 2411 which has no spectral classification.

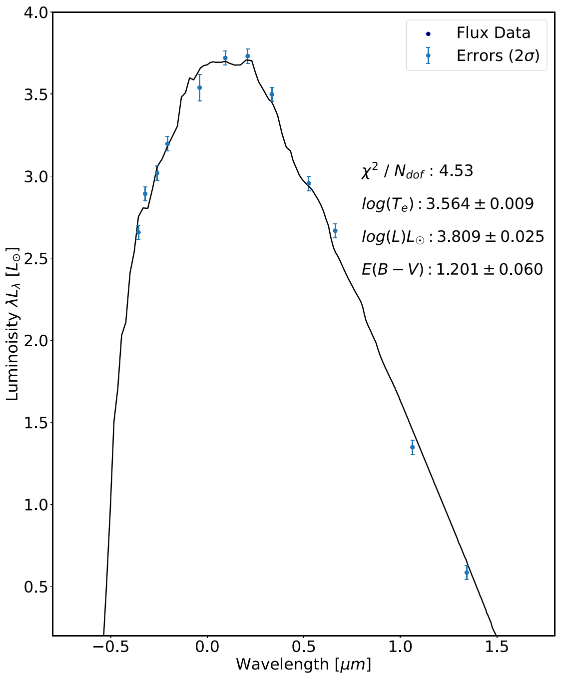

Figure A5. The SED of long period variable candidate star IRAS 5361–2406. It has no spectral classification.

APPENDIX B: DERIVATION OF EQUATION (2)

We start with equation (1), for a constant star formation rate of stars with masses $M > M_{\rm min}$, and a mean mass of $\langle M\rangle = (x-1)M_{min}/(x-2)$. If we integrate over M, we get the number of stars

$$N = \int_{t_{\rm min}}^{t_{\rm max}} \int_{M_{\rm min}}^{\infty} dM \frac{dn}{dMdt} = \frac{SFR}{\langle M\rangle}\Delta t.$$

For an interval of ages where $\Delta t = t_{\rm max} - t_{\rm min}$, the number of stars dying within a time period δt is

$$\int_{t_{\rm min}}^{t_{\rm max}} dt \int_{M(t)}^{M(t+\delta t)} dM \frac{dn}{dMdt},$$

where $M(t)$ is the mass of a star dying at time t. If we do the mass integral, we get

$$\int_{t_{\rm min}}^{t_{\rm max}} dt \frac{SFR}{\langle M\rangle}\left[\left(\frac{M(t)}{M_{\rm min}}\right)^{1-x} - \left(\frac{M(t+\delta t)}{M_{\rm min}}\right)^{1-x}\right].$$

and then Taylor expand $M(t+\delta t) = M(t) + (dM/dt)\delta t$ to get

$$\int_{t_{\rm min}}^{t_{max}} dt \frac{SFR}{\langle M\rangle}\frac{dM}{dt}\left(\frac{M(t)}{M_{\rm min}}\right)^{-x}(x-1)\delta t.$$

We transform the integral, by change of variables, from time t to mass M,

$$\int_{M(t_{\rm min})}^{M(t_{\rm max})} dM \frac{SFR}{\langle M\rangle}\left(\frac{M(t)}{M_{\rm min}}\right)^{-x}(x-1)\delta t,$$

and then carry out the integral to obtain equation (2).

This paper has been typeset from a TEX/LATEX file prepared by the author.